Supplementary Material for: Fermionic-propagator and alternating-basis quantum Monte Carlo methods for correlated electrons on a lattice

Veljko Janković[1, a)] and Jakša Vučičević[1, b)]
Institute of Physics Belgrade, University of Belgrade, Pregrevica 118, 11080 Belgrade, Serbia

SI. FPQMC METHOD: MONTE CARLO UPDATES

Here, we present the Monte Carlo updates we use to move through the configuration space of our FPQMC method.

The configuration space is sampled through Markov chains starting from an, in principle arbitrary, configuration $\mathcal{C}_0$. The Metropolis–Hastings algorithm is used to determine the probability of transferring from configuration $\mathcal{C}_n$ at Monte Carlo step n to configuration $\mathcal{C}_{n+1}$ at the subsequent Monte Carlo step $n+1$. The transition probability $W_{n\to n+1}$ is

$$W_{n\to n+1} = W^{\text{prop}}_{n\to n+1} W^{\text{acc}}_{n\to n+1} \tag{S1}$$

where $W^{\text{prop}}_{n\to n+1}$ is the probability of proposing the update from configuration $\mathcal{C}_n$ to configuration $\mathcal{C}_{n+1}$, while $W^{\text{acc}}_{n\to n+1}$ determines the probability with which such a proposal is accepted. The Metropolis–Hastings acceptance rate reads as

$$W^{\text{acc}}_{n\to n+1} = \min\{1, R_{n\to n+1}\} \tag{S2}$$

where the acceptance ratio $R_{n\to n+1} = 1/R_{n+1\to n}$ depends on the weights of the configurations involved, as well as on the proposal probabilities in both directions $\mathcal{C}_n \leftrightarrow \mathcal{C}_{n+1}$ in the following manner

$$R_{n\to n+1} = \frac{w(\mathcal{C}_{n+1}) W^{\text{prop}}_{n+1\to n}}{w(\mathcal{C}_n) W^{\text{prop}}_{n\to n+1}}. \tag{S3}$$

A. Updates that conserve the number of particles

1. `change_r_local`
   We randomly choose one real-space state $|\Psi^n_{i,l_0}\rangle$ [in all the time-dependent computations we perform, $l_0 \neq 1$ due to $|\Psi^n_{i,1}\rangle \equiv |\psi(0)\rangle$ at each Monte Carlo step n] and move an arbitrarily chosen electron (spin σ, position $\mathbf{r}^\sigma_j$) to a new position $\mathbf{s}^\sigma_j$ under the condition that the state $(\sigma, \mathbf{s}^\sigma_j)$ is unoccupied in $|\Psi^n_{i,l_0}\rangle$.

   The inverse move proceeds in the same manner as described above. The ratio of proposal weights is $\dfrac{W^{\text{prop}}_{n+1\to n}}{W^{\text{prop}}_{n\to n+1}} = 1$.

   This move ensures that we sample configurations with different real-space electron patterns.

2. `change_r_global`
   We randomly choose one real-space state $|\Psi^n_{i,l_0}\rangle$ [in all the time-dependent computations we perform, $l_0 \neq 1$ due to $|\Psi^n_{i,1}\rangle \equiv |\psi(0)\rangle$ at each Monte Carlo step n] and replace it by a new state $|\Psi^{n+1}_{i,l_0}\rangle \neq |\Psi^n_{i,l_0}\rangle$. While the effects of this "global" move can be mimicked by multiple applications of its "local" version `change_r_local`, we found this move very useful in evenly sampling the configuration space, especially in time-dependent FPQMC simulations.

3. `spin_flip`—*used only in equilibrium FPQMC simulations because it does not separately conserve the number of spin-up and spin-down electrons, yet it conserves the total electron number*
   We randomly choose spin σ and attempt to increase/decrease the number of electrons of spin $\sigma/\overline{\sigma}$ by one.

[a)] veljko.jankovic@ipb.ac.rs
[b)] jaksa.vucicevic@ipb.ac.rs

In each imaginary-time slice $l = 1, \ldots, N_\tau$, we choose an electron of spin σ at position $\mathbf{r}$ from the real-space state $|\Psi^n_{i,l}\rangle$ and construct the real-space state $|\Psi^{n+1}_{i,l}\rangle$ by changing the electron's position $\mathbf{r} \to \mathbf{s}$ and spin $\sigma \to \overline{\sigma}$. The ratio of the proposal probabilities in the real space can be directly computed as $\left(\frac{W^{\mathrm{prop}}_{n+1\to n}}{W^{\mathrm{prop}}_{n\to n+1}}\right)_{i,l} = \frac{N_\sigma(N_c - N_{\overline{\sigma}})}{(1+N_{\overline{\sigma}})(N_c - N_\sigma + 1)}$, where N_σ and $N_{\overline{\sigma}}$ are numbers of electrons of spin σ and $\overline{\sigma}$ in $|\Psi^n_{i,l}\rangle$.

This move is very useful once the FPQMC starts sampling configurations whose total electron number (the sum of the numbers of spin-up and spin-down electrons) fluctuates around the value predicted by the fixed temperature and chemical potential. One value of the total electron number may be realized via many different combinations of numbers of spin-up and spin-down electrons, and it is precisely this move that enables efficient sampling through all these combinations.

B. Updates that do not conserve the number of particles

The updates `add_particle` and `remove_particle` are used only in equilibrium FPQMC simulations, when the number of particles fluctuates according to the fixed chemical potential and temperature.

The move `add_particle`/`remove_particle` adds/removes one electron from the configuration. These two moves are inverses of one another and their acceptance rates are mutually equal. The spin σ of the electron added to/removed from the imaginary-time slice $l = 1$ fixes that an electron added to/removed from the remaining imaginary-time slices $l = 2, \ldots, N_\tau$ must have the same spin σ.

Let N_σ denote the number of electrons of spin σ in state $|\Psi^n_{i,l}\rangle$ (before the update). In the first imaginary-time slice $l = 1$, an electron can be added to any of $N_c - N_\uparrow + N_c - N_\downarrow$ empty single-particle states, while an electron can be removed from any of $N_\uparrow + N_\downarrow$ occupied single-particle states. Concerning the inverse move, an electron can be removed from any of $N_\uparrow + N_\downarrow + 1$ occupied single-particle states, while an electron can be added to any of $2N_c - N_\uparrow - N_\downarrow + 1$ empty single-particle states. We thus have

$$\left(\frac{W^{\mathrm{prop}}_{n+1\to n}}{W^{\mathrm{prop}}_{n\to n+1}}\right)^{\mathrm{add}}_{i,l=1} = \frac{2N_c - N_\uparrow - N_\downarrow}{N_\uparrow + N_\downarrow + 1}, \quad \left(\frac{W^{\mathrm{prop}}_{n+1\to n}}{W^{\mathrm{prop}}_{n\to n+1}}\right)^{\mathrm{rmv}}_{i,l=1} = \frac{N_\uparrow + N_\downarrow}{2N_c - N_\uparrow - N_\downarrow + 1}. \tag{S4}$$

In all other imaginary-time slices $l = 2, \ldots, N_\tau$, we have

$$\left(\frac{W^{\mathrm{prop}}_{n+1\to n}}{W^{\mathrm{prop}}_{n\to n+1}}\right)^{\mathrm{add}}_{i,l\geq 2} = \frac{N_c - N_\sigma}{N_\sigma + 1}, \quad \left(\frac{W^{\mathrm{prop}}_{n+1\to n}}{W^{\mathrm{prop}}_{n\to n+1}}\right)^{\mathrm{rmv}}_{i,l\geq 2} = \frac{N_\sigma}{N_c - N_\sigma + 1}. \tag{S5}$$

C. Fast determinant updates

The determinant $\mathcal{D}_\beta(\mathcal{C}, \Delta\tau)$ is a product of $2N_\tau$ determinants of imaginary-time single-particle propagators on a lattice. Since all the updates can be seen as a single row/column change or addition/removal of a single row/column, changes in individual determinants may be efficiently computed using the formulae for fast determinant updates. These formulae, which provide the determinant ratio before and after the update, deal with the inverses of the corresponding matrices. We store these inverses in memory and recompute them from scratch each time a Monte Carlo update is accepted.

D. Extraction of Monte Carlo results

The average sign of FPQMC simulations is relatively large, so that, after the initial equilibration phase, the physical quantities we compute depend quite weakly on the number of Monte Carlo steps completed. All relevant quantities are measured at every Monte Carlo step, and the individual-step data are grouped into bins of length L_b, where $L_b \sim 10^4 - 10^5$, depending on the total number of steps completed. To provide the best possible estimate of a quantity, we discard the first 80% of the simulation. The average of the binned data in the last 20% of the simulation is taken as the Monte Carlo estimate of the quantity of interest. The statistical error is estimated as the root-mean-square deviation of the binned data in the final 20% of the simulation from the above-computed average value. Such an estimate of the error is appropriate for statistically independent data. While we have not performed a systematic binning analysis, we may expect that the bin length we chose is sufficiently large that the data from different bins may be considered as statistically independent.

SII. ABQMC METHOD IN REAL TIME: MONTE CARLO UPDATES

Here, we present the Monte Carlo updates we use to move through the configuration space of our real-time ABQMC method to compute the survival probability of an initial (pure) state. We only need updates that conserve the number of particles of each spin orientation.

Within the alternating-basis method, which employs both coordinate-space and momentum-space many-body states, we perform individual Monte Carlo updates on one of the two sets of states. The updates changing coordinate-space states are the updates `change_r_local` and `change_r_global` that we present in Sec. SI. The updates that change momentum-space states are designed so as to respect the momentum-conservation law. While the proposal probabilities $W^{\mathrm{prop}}_{n\to n+1}$ for coordinate-space updates can be determined relatively straightforwardly (even analytically), see Sec. SI, their determination for the momentum-space updates may be quite challenging due to the explicit momentum conservation. For all such moves, we can give no analytical expression for $W^{\mathrm{prop}}_{n\to n+1}$, and we have to devise computer algorithms capable of precisely enumerating all possible propositions that comply with the momentum (and also particle-number) conservation.

1. `add_q`
   The momentum $\mathbf{K}$ of each of the states $|\Psi^n_{k,l}\rangle$, $l = 1, \ldots, N_{\tau/t}$, is increased by a randomly chosen momentum $\mathbf{q} \neq 0$, thereby obtaining new states $|\Psi^{n+1}_{k,l}\rangle$, $l = 1, \ldots, N_{\tau/t}$, with momentum $\mathbf{K} + \mathbf{q}$. The real-space states are not changed, i.e., $|\Psi^n_{i,l}\rangle = |\Psi^{n+1}_{i,l}\rangle$. In each momentum-space state, momentum $\mathbf{q}$ is added to an electron of spin σ that carries momentum $\mathbf{k}^\sigma_{j,l}$ under the condition that the state $(\sigma, \mathbf{k}^\sigma_{j,l} + \mathbf{q})$ is unoccupied in $|\Psi^n_{k,l}\rangle$. All possible momentum-accepting states $(\sigma, \mathbf{k}^\sigma_{j,l})$ have to be explicitly enumerated and their number is denoted as $p_l^{+\mathbf{q}}$.

   The inverse move starts from states $|\Psi^{n+1}_{k,l}\rangle$, $l = 1, \ldots, N_{\tau/t}$, with momentum $\mathbf{K} + \mathbf{q}$, and adds momentum $-\mathbf{q}$ to each of them. All possible momentum-accepting states in $|\Psi^{n+1}_{k,l}\rangle$ have to be explicitly enumerated and their number is denoted as $p_l^{-\mathbf{q}}$.

   The ratio of the proposal probabilities is then $\dfrac{W^{\mathrm{prop}}_{n+1\to n}}{W^{\mathrm{prop}}_{n\to n+1}} = \displaystyle\prod_l \frac{p_l^{+\mathbf{q}}}{p_l^{-\mathbf{q}}}$.

   This move ensures that we sample configurations from sectors featuring different electronic momenta.

2. `exchange_q`
   We randomly choose one momentum-space state $|\Psi^n_{k,l_0}\rangle$ in which we select two electrons of spins σ_1 and σ_2 and momenta $\mathbf{k}^{\sigma_1}_{j_1}$ and $\mathbf{k}^{\sigma_2}_{j_2}$, which are ordered so that $k_{j_1,y} + N_y k_{j_1,x} > k_{j_2,y} + N_y k_{j_2,x}$. The momenta are subsequently changed using $\mathbf{k}^{\sigma_1}_{j_1} \to \mathbf{k}^{\sigma_1}_{j_1} + \mathbf{q}$, $\mathbf{k}^{\sigma_2}_{j_2} \to \mathbf{k}^{\sigma_2}_{j_2} - \mathbf{q}$ ($\mathbf{q} \neq 0$). As a consequence, the net momentum of $|\Psi^n_{k,l_0}\rangle$ remains unchanged. Obviously, the move may be realized only when the states $(\sigma_1, \mathbf{k}^{\sigma_1}_{j_1} + \mathbf{q})$ and $(\sigma_2, \mathbf{k}^{\sigma_2}_{j_2} - \mathbf{q})$ are both unoccupied in $|\Psi^n_{k,l_0}\rangle$.

   We note that enumerating all possible momenta $\mathbf{q} \neq 0$ that may be transferred between the electrons is relatively simple for $\sigma_1 \neq \sigma_2$ ($\sigma_2 = \overline{\sigma_1}$), when the two electrons can be distinguished by their spins. It is then enough to go through all empty states $(\sigma_1, \mathbf{k}')$ to which the electron $(\sigma_1, \mathbf{k}^{\sigma_1}_{j_1})$ can be moved and to determine the corresponding momentum transfer $\mathbf{q} = \mathbf{k}' - \mathbf{k}^{\sigma_1}_{j_1}$. We then ask if the state $(\overline{\sigma_1}, \mathbf{k}^{\overline{\sigma}_1}_{j_2} - \mathbf{q})$ is empty; in the affirmative case, we memorize the current $\mathbf{q}$ as one possible momentum transfer. The inverse move proceeds in a completely analogous manner by explicitly enumerating possible back-transfers.

   On the other hand, two electrons of the same spin are indistinguishable, and special care should be exercised to avoid double counting. For given $\mathbf{k}_{j_1}$ and $\mathbf{k}_{j_2}$ (we now omit $\sigma_1 = \sigma_2$), possible values of $\mathbf{q}$ follow from the construction that is schematically summarized in Fig. S1. We make use of the periodic boundary conditions to construct a new unit cell (in the momentum space) such that the electron of momentum $\mathbf{k}_{j_1}$ is in its "center", while its vertices are at $\mathbf{k}_{j_2}$ and its periodic copies $\mathbf{k}_{j_2} + 2\pi(1,0)$, $\mathbf{k}_{j_2} + 2\pi(0,1)$, and $\mathbf{k}_{j_2} + 2\pi(1,1)$. The "central point" and the four vertices partition the unit cell into four rectangular regions that are colored yellow (bottom left), green (top left), cyan (top right), and magenta (bottom right). The vectors $\mathbf{q}$ that may be added to $\mathbf{k}_{j_1}$ and subtracted from $\mathbf{k}_{j_2}$ are to be selected so that the final states $\mathbf{k}_{j_1} + \mathbf{q}$ and $\mathbf{k}_{j_2} - \mathbf{q}$ belong to just one half of each of the regions, the two halves being separated by the line connecting the "central" point and the vertices. The halves from which possible final states $\mathbf{k}_{j_1} + \mathbf{q}$, and thus possible momentum transfers $\mathbf{q}$, are selected is shaded. Choosing the momentum transfer such that the final state $\mathbf{k}_{j_1} + \mathbf{q}$ belongs to the other (unshaded) half is equivalent to assigning momentum $\mathbf{k}_{j_1}$ to the blue electron and $\mathbf{k}_{j_2}$ to the red electron, i.e., to exchanging momentum labels $\mathbf{k}_{j_1}$ and $\mathbf{k}_{j_2}$, which produces the setup equivalent to that presented in Fig. S1. The momentum transfer $\mathbf{q}$

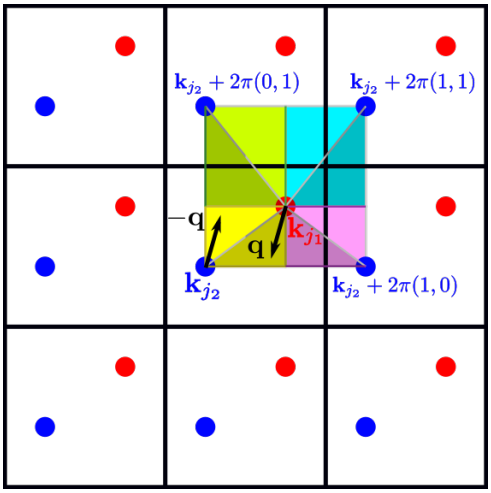

Figure S1. Construction used to correctly enumerate all possible momenta $\mathbf{q} \neq 0$ that can be exchanged between two electrons of equal spins that carry momenta $\mathbf{k}_{j_1}$ and $\mathbf{k}_{j_2}$. The momenta $\mathbf{q}$ that may be added to $\mathbf{k}_{j_1}$ (and subtracted from $\mathbf{k}_{j_2}$) are such that the final state $\mathbf{k}_{j_1} + \mathbf{q}$ is found in one of the four shaded triangles, while $\mathbf{k}_{j_2} - \mathbf{q}$ is found in one of the four unshaded triangles.

along the edges of the four shaded triangles should be counted only once because of the periodic boundary conditions. For example, if we enumerate possible $\mathbf{q}$s along the vertical edge of the green shaded triangle, then we should not enumerate possible $\mathbf{q}$s along the vertical edge of the cyan shaded triangle. Moreover, if any of the lines connecting the "center" and the four edges contains any other lattice point, possible $\mathbf{q}$s along that line are subjected to the condition $|\mathbf{q}| \leq |\mathbf{k}_{j_1} - \mathbf{k}_{j_2} - 2\pi(a_x, a_y)|/2$, where $(a_x, a_y) \in \{(0,0), (1,0), (0,1), (1,1)\}$. While this construction is appropriate for $k_{j_1,x} \neq k_{j_2,x}$ and $k_{j_1,y} \neq k_{j_2,y}$, further discussion is needed when either $k_{j_1,x} = k_{j_2,x}$ or $k_{j_1,y} = k_{j_2,y}$. In the inverse move, we start from the two electrons carrying momenta $\mathbf{k}'_{j_1} = \mathbf{k}_{j_1} + \mathbf{q}$ and $\mathbf{k}'_{j_2} = \mathbf{k}_{j_2} - \mathbf{q}$, we order them so that $k'_{j_1,y} + N_y k'_{j_1,x} > k'_{j_2,y} + N_y k'_{j_2,x}$, and repeat the above-described procedure.

This move ensures that we sample configurations belonging to the sector of the chosen total electron momentum.

SIII. DETAILED PERFORMANCE OF THE FPQMC METHOD APPLIED TO EVALUATE THE EQUATION OF STATE

A. $U/J = 4$, $T/J = 1.0408$

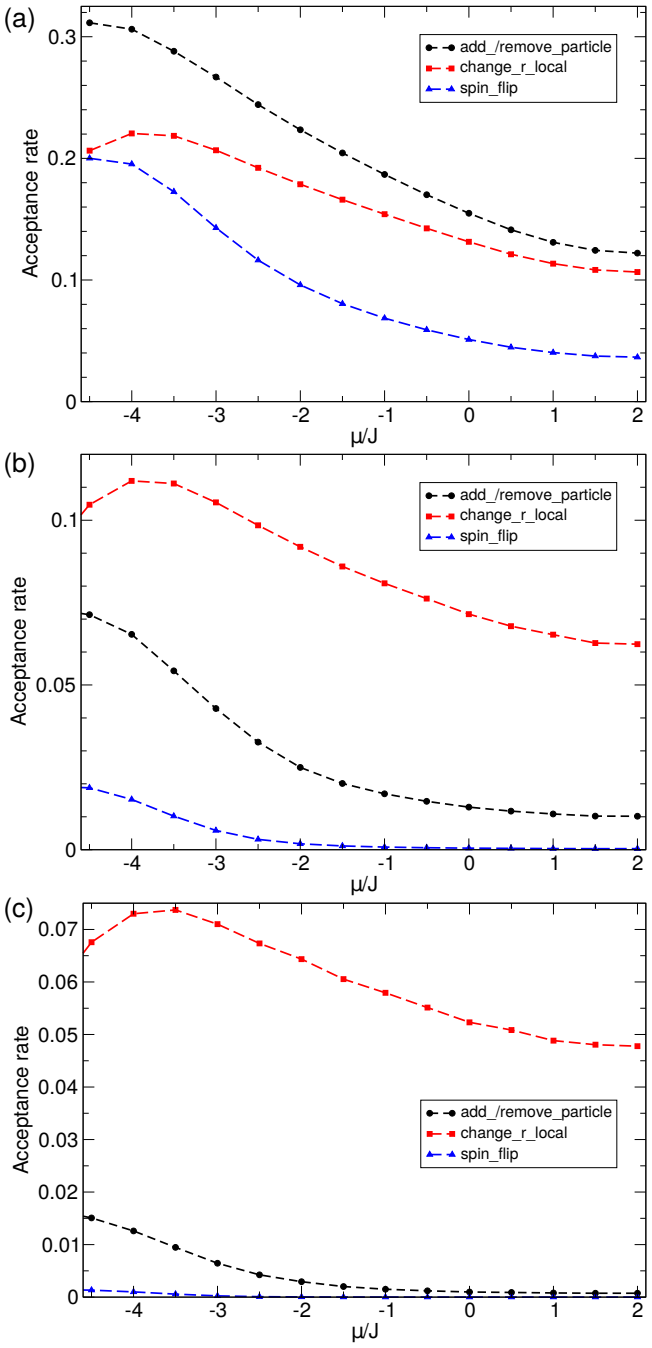

Figure S2. Acceptance rates of individual moves as a function of the chemical potential. FPQMC simulations are performed on a 4×4 square-lattice cluster using (a) $N_\tau = 2$, (b) $N_\tau = 4$, and (c) $N_\tau = 6$ imaginary-time slices. The remaining parameters are: $U/J = 4$, $T/J = 1.0408$. Acceptance rates generally decrease with N_τ and with the filling (chemical potential).

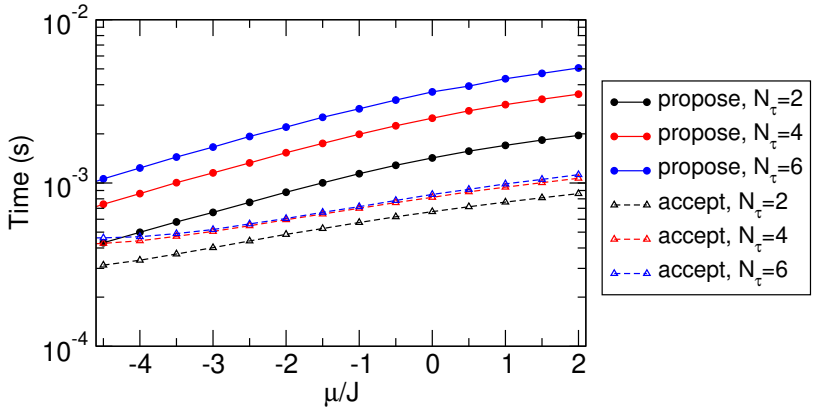

Figure S3. Average time needed to propose (full symbols connected by solid lines) and accept (empty symbols connected by dashed lines) a Monte Carlo update as a function of the chemical potential. FPQMC simulations are performed on a 4×4 square-lattice cluster with different numbers of imaginary-time slices N_τ. The remaining parameters are: $U/J = 4$, $T/J = 1.0408$.

B. $U/J = 24$, $T/J = 1.0408$

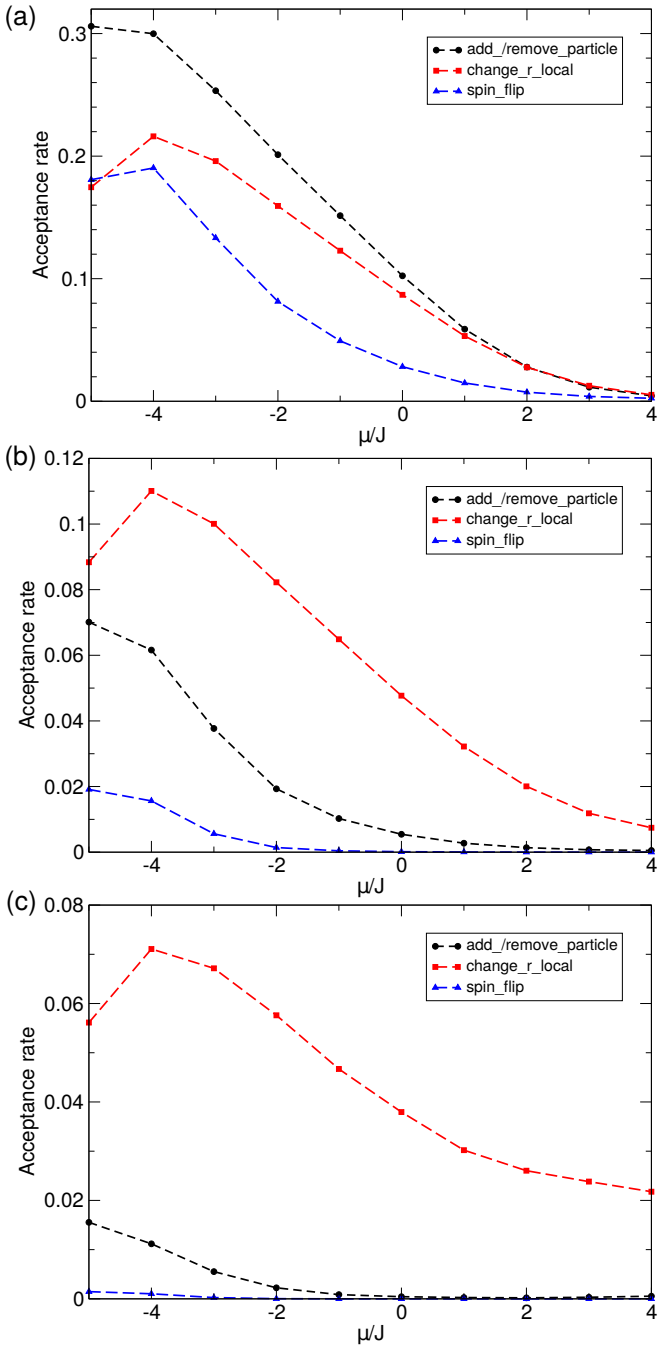

Figure S4. Acceptance rates of individual moves as a function of the chemical potential. FPQMC simulations are performed on a 4×4 square-lattice cluster using (a) $N_\tau = 2$, (b) $N_\tau = 4$, and (c) $N_\tau = 6$ imaginary-time slices. The remaining parameters are: $U/J = 24$, $T/J = 1.0408$. Acceptance rates generally decrease with N_τ and with the filling (chemical potential).

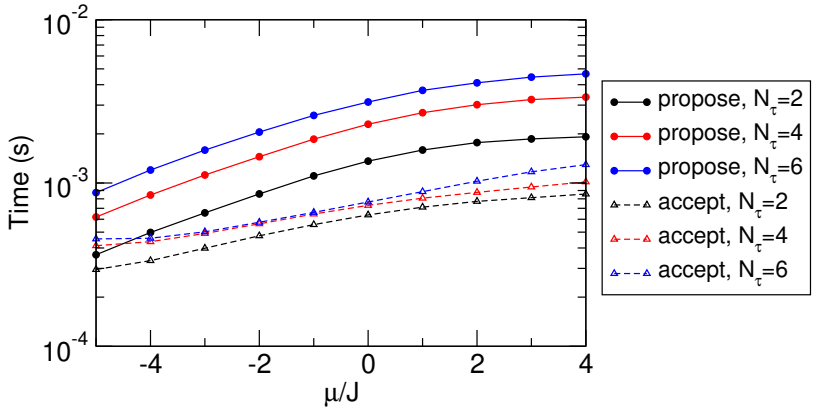

Figure S5. Average time needed to propose (full symbols connected by solid lines) and accept (empty symbols connected by dashed lines) an MC update as a function of the chemical potential. FPQMC simulations are performed on a 4×4 square-lattice cluster with different numbers of imaginary-time slices N_τ. The remaining parameters are: $U/J = 24$, $T/J = 1.0408$.

SIV. ABQMC METHOD APPLIED TO EQUILIBRIUM SITUATIONS

Here, we derive the ABQMC method in equilibrium situations (Sec. SIV A) and present our implementation of the method (Sec. SIV B). Since the ABQMC method is equally adept at calculating quantities in real and momentum space, we complement the results presented in Fig. 7 of the main text by presenting the momentum distribution at different fillings (Sec. SIV C). We conclude in Sec. SIV D by discussing acceptance rates and proposal/acceptance times of MC updates introduced in Sec. SIV B.

A. ABQMC method in equilibrium: Basic equations

Dividing the imaginary-time interval $[0,\beta]$ into N_τ slices of length $\Delta\tau \equiv \beta/N_\tau$, employing the lowest-order STD, and inserting the spectral decompositions of H_0 and $H_{\rm int}$, we find the following ABQMC approximant for the partition function at temperature $T = 1/\beta$:

$$Z \approx \sum_{\mathcal{C}} \mathcal{D}(\mathcal{C}) e^{-\Delta\tau\varepsilon(\mathcal{C})}. \tag{S6}$$

The configuration

$$\mathcal{C} = \{|\Psi_{k,1}\rangle, \ldots, |\Psi_{k,N_\tau}\rangle, |\Psi_{i,1}\rangle, \ldots, |\Psi_{i,N_\tau}\rangle\} \tag{S7}$$

resides on the contour depicted in Fig. 1(a) of the main text and consists of N_τ Fock states $|\Psi_{k,l}\rangle$ ($l = 1, \ldots, N_\tau$) in the momentum representation and N_τ Fock states $|\Psi_{i,l}\rangle$ in the coordinate representation. $\mathcal{D}(\mathcal{C})$ is the product of $2N_\tau$ Slater determinants

$$\mathcal{D}(\mathcal{C}) \equiv \prod_{l=1}^{N_\tau} \langle \Psi_{i\oplus 1,l}|\Psi_{k,l}\rangle\langle\Psi_{k,l}|\Psi_{i,l\ominus 1}\rangle \tag{S8}$$

that stem from the sequence of basis alternations between the momentum and coordinate eigenbasis. The symbol $\varepsilon(\mathcal{C})$ stands for

$$\varepsilon(\mathcal{C}) \equiv \sum_{l=1}^{N_\tau} \left[\varepsilon_0(\Psi_{k,l}) + \varepsilon_{\rm int}(\Psi_{i,l})\right]. \tag{S9}$$

The equilibrium expectation value an observable A_a diagonal in either coordinate ($a = i$) or momentum ($a = k$) representation reads as

$$\langle A_a\rangle \approx \frac{1}{Z}\sum_{\mathcal{C}} \mathcal{D}(\mathcal{C}) e^{-\Delta\tau\varepsilon(\mathcal{C})} \frac{1}{N_\tau}\sum_{l=1}^{N_\tau} \mathcal{A}_a(\Psi_{a,l}), \tag{S10}$$

where

$$\mathcal{A}_a(\Psi_{a,l}) \equiv \langle\Psi_{a,l}|A_a|\Psi_{a,l}\rangle. \tag{S11}$$

The evaluation of Eq. (S10) using the importance-sampling MC procedure is complicated by the fact that $\mathcal{D}(\mathcal{C})$ is a complex number defined by its modulus and phase. While the modulus can be included in the weight of configuration $\mathcal{C}$, the phase gives rise to the so-called phase problem, which is generally much harder to curb than the ordinary sign problem. However, since the STD preserves the equality $Z = Z^*$,[1] Eq. (S6) can be replaced by

$$Z \approx \sum_{\mathcal{C}} {\rm Re}\{\mathcal{D}(\mathcal{C})\}\, e^{-\Delta\tau\varepsilon(\mathcal{C})}, \tag{S12}$$

and we remain with the ordinary sign problem. Equation (S10) should then be replaced by

$$\langle A_a\rangle \approx \frac{\sum_{\mathcal{C}} {\rm Re}\{\mathcal{D}(\mathcal{C})\}\, e^{-\Delta\tau\varepsilon(\mathcal{C})} \frac{1}{N_\tau}\sum_{l=1}^{N_\tau} \mathcal{A}_a(\Psi_{a,l})}{\sum_{\mathcal{C}} {\rm Re}\{\mathcal{D}(\mathcal{C})\}\, e^{-\Delta\tau\varepsilon(\mathcal{C})}}. \tag{S13}$$

Defining the weight $w(\mathcal{C})$ of configuration $\mathcal{C}$ as

$$w(\mathcal{C}) \equiv |\mathrm{Re}\{\mathcal{D}(\mathcal{C})\}| e^{-\Delta\tau\varepsilon(\mathcal{C})}, \tag{S14}$$

Eq. (S13) is rewritten as

$$\langle A_a \rangle \approx \frac{\left\langle \mathrm{sgn}(\mathcal{C}) \frac{1}{N_\tau} \sum_{l=1}^{N_\tau} \mathcal{A}_a(\Psi_{a,l}) \right\rangle_w}{\langle \mathrm{sgn}(\mathcal{C}) \rangle_w} \tag{S15}$$

where $\langle \dots \rangle_w$ denotes the weighted average over all $\mathcal{C}$ with respect to the weight $w(\mathcal{C})$; $\mathrm{sgn}(\mathcal{C}) \equiv \mathrm{Re}\{\mathcal{D}(\mathcal{C})\}/|\mathrm{Re}\{\mathcal{D}(\mathcal{C})\}|$ is the sign of configuration $\mathcal{C}$, while $|\langle \mathrm{sgn} \rangle| \equiv |\langle \mathrm{sgn}(\mathcal{C}) \rangle_w|$ is the average sign of the ABQMC simulation.

B. ABQMC method in equilibrium: Monte Carlo updates

Apart from previously introduced updates `change_r_local` and `change_r_global` in real space (Sec. SI) and `add_q` and `exchange_q` in momentum space (Sec. SII), we need updates that insert/remove a particle, which are different from their counterparts in Sec. SI.

The ABQMC move `add_particle`/`remove_particle` adds/removes one electron from the configuration. These two moves are inverses of one another. While analogous moves are relatively simply implemented in the FPQMC algorithm, here, special care is to be exercised because of the particle-number and momentum conservation. In more detail, the spin σ of the electron added to/removed from the imaginary-time slice $l = 1$ fixes that an electron added to/removed from the remaining imaginary-time slices $l = 2, \dots, N_\tau$ must have the same spin σ. Furthermore, the momentum $\mathbf{q}$ of the electron added to/removed from the imaginary-time slice $l = 1$ fixes that momentum change upon addition/removal of an electron in the remaining imaginary-time slices $l = 2, \dots, N_\tau$ must be precisely $\mathbf{q}$. This requirement may be realized in many different ways. One trivial possibility is to add/remove the electron to/from the state $(\sigma, \mathbf{q})$ if this state is empty/occupied. On the other hand, we may add/remove the electron to/from state $(\sigma, \mathbf{k})$, in which case we should find another electron $(\sigma_{\mathrm{comp}}, \mathbf{k}_{\mathrm{comp}})$ (of arbitrary spin σ_{comp}) to compensate for the difference in the momentum change from $\pm\mathbf{q}$, where $+/-$ sign is for electron addition/removal. The electron in the state $(\sigma_{\mathrm{comp}}, \mathbf{k}_{\mathrm{comp}})$ that may receive the momentum difference $\pm(\mathbf{q} - \mathbf{k})$ will be termed the compensating electron. The situation is relatively simple when the spin of the compensating electron is $\overline{\sigma}$ because the added electron and the compensating electron may be distinguished by their spins. When the spins of the added and compensating electrons are both equal to σ, these two electrons cannot be distinguished in the sense that their roles (added/compensating) may be reverted. Special care should thus be taken to avoid double counting. An elaborate analysis reveals that the double counting is avoided by ordering the momenta of:

(`add`) the added electron $\mathbf{k}$ and the compensating electron $\mathbf{k}_{\mathrm{comp}} + \mathbf{q} - \mathbf{k}$ after the compensation;

(`rmv`) the removed electron $\mathbf{k}$ and the compensating electron $\mathbf{k}_{\mathrm{comp}}$ before the compensation.

The ordering is the same as in the update `exchange_q`.

While the above discussion regards the momentum-space states $|\Psi^n_{k,l}\rangle \to |\Psi^{n+1}_{k,l}\rangle$, the situation with the real-space states $|\Psi^n_{i,l}\rangle \to |\Psi^{n+1}_{i,l}\rangle$ is far less complicated because only the particle-number conservation should be satisfied. The spin of the electron to be added to/removed from from each $|\Psi^n_{i,l}\rangle$ is determined by the spin of the electron added to/removed from $|\Psi^n_{k,0}\rangle$. The ratio of the backward and forward proposal probabilities for the real-space parts of the configuration may be directly computed as:

$$(\texttt{add}) \quad \left(\frac{W^{\mathrm{prop}}_{n+1\to n}}{W^{\mathrm{prop}}_{n\to n+1}} \right)_{i,l} = \frac{N_c - N_\sigma}{1 + N_\sigma},$$

$$(\texttt{rmv}) \quad \left(\frac{W^{\mathrm{prop}}_{n+1\to n}}{W^{\mathrm{prop}}_{n\to n+1}} \right)_{i,l} = \frac{N_\sigma}{N_c - N_\sigma + 1},$$

where N_σ is the number of electrons of spin σ in all the states $|\Psi^n_{i/k,l}\rangle$ (before the update).

There are also some differences in the move `spin_flip`, in which we randomly choose spin σ and attempt to increase/decrease the number of electrons of spin $\sigma/\overline{\sigma}$ by one.

In each imaginary-time slice $l = 1, \dots, N_\tau$, we explicitly enumerate the momentum states $(\sigma, \mathbf{k}) \in |\Psi^n_{k,l}\rangle$ such that $(\overline{\sigma}, \mathbf{k}) \notin |\Psi^n_{k,l}\rangle$. This is the simplest possible update that changes the spin of an electron and yet keeps the

total momentum of the configuration fixed. The state $|\Psi^{n+1}_{k,l}\rangle$ is then obtained from the state $|\Psi^{n}_{k,l}\rangle$ by removing the electron in the state $(\sigma, \mathbf{k})$ and adding the electron in the state $(\overline{\sigma}, \mathbf{k})$. The inverse move proceeds in an analogous manner: we explicitly enumerate momentum the states $(\overline{\sigma}, \mathbf{k}') \in |\Psi^{n+1}_{k,l}\rangle$ such that $(\sigma, \mathbf{k}') \notin |\Psi^{n+1}_{k,l}\rangle$.

In each imaginary-time slice $l = 1, \ldots, N_\tau$, we choose an electron of spin σ at position $\mathbf{r}$ from the real-space state $|\Psi^{n}_{i,l}\rangle$ and construct the real-space state $|\Psi^{n+1}_{i,l}\rangle$ by changing the electron's position $\mathbf{r} \to \mathbf{s}$ and spin $\sigma \to \overline{\sigma}$. The ratio of the proposal probabilities in the real space can be directly computed as $\left(\frac{W^{\mathrm{prop}}_{n+1\to n}}{W^{\mathrm{prop}}_{n\to n+1}}\right)_{i,l} = \frac{N_\sigma(N_c - N_{\overline{\sigma}})}{(1+N_{\overline{\sigma}})(N_c - N_\sigma + 1)}$, where N_σ and $N_{\overline{\sigma}}$ are numbers of electrons of spin σ and $\overline{\sigma}$ in $|\Psi^{n}_{i/k,l}\rangle$.

C. ABQMC method in equilibrium: Numerical results

Within the ABQMC method, coordinate and momentum bases are treated symmetrically, meaning that the method should be equally adept at calculating quantities diagonal in these two bases. As an example applications in the momentum space, in Fig. S6 we show the momentum distribution, $\frac{1}{2}\sum_\sigma \langle n_{\mathbf{k}\sigma}\rangle$, in the same setup as in Fig. 4 of the main text ($U/J = 4$, $T/J = 1.0408$).

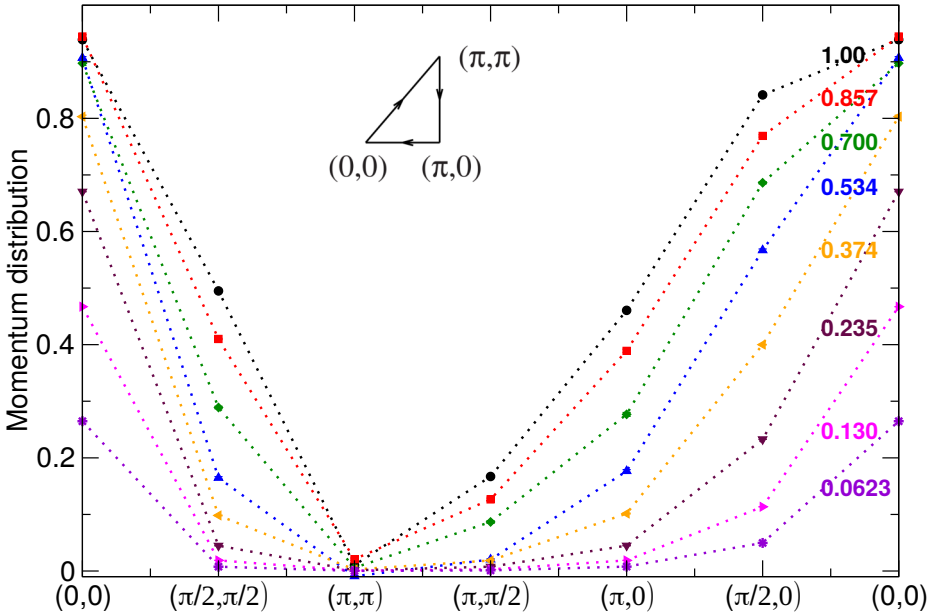

Figure S6. Momentum distribution, $\frac{1}{2}\sum_\sigma \langle n_{\mathbf{k}\sigma}\rangle$, for different fillings ρ_e (half filling is $\rho_e = 1$) computed using the equilibrium ABQMC approach on a 4×4 square-lattice cluster. Model parameters are $U/J = 4$, $T/J = 1.0408$, while μ/J is varied from 2 to -5. The pathway through the irreducible Brillouin zone is summarized in the inset. Cited values of ρ_e are from Ref. 2. Dotted lines serve as guides to the eye. Statistical error bars are generally smaller than symbol size.

D. ABQMC method in equilibrium: Acceptance rates and proposal/acceptance times

1. $U/J = 4$, $T/J = 1.0408$

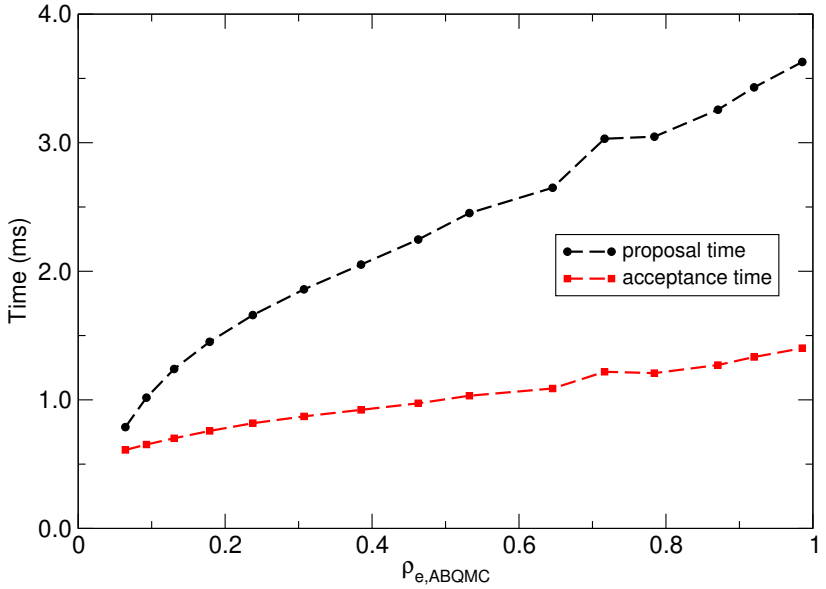

Figure S7. Average time needed to propose (black circles) and accept (red squares) one Monte Carlo update as a function of the ABQMC electron density. The averaging is performed over all updates used in ABQMC simulations to evaluate the equation of state: `add_particle`, `remove_particle`, `spin_flip`, `add_q`, `exchange_q`, `change_r_local`, and `change_r_global`.

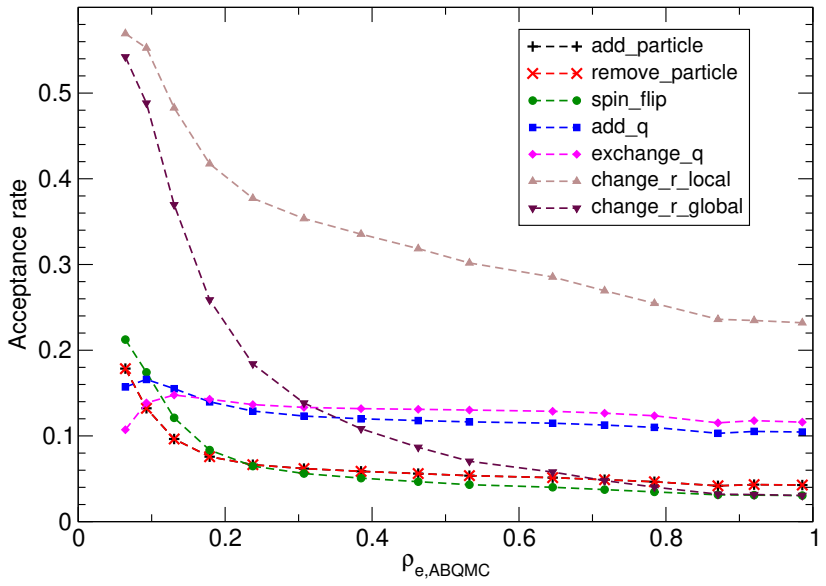

Figure S8. Acceptance rates of individual Monte Carlo updates as a function of the ABQMC electron density. Being inverses of one another, the acceptance rates of moves `add_particle` and `remove_particle` are mutually equal. The acceptance rates of moves `add_particle`, `remove_particle`, `spin_flip`, `add_q`, and `exchange_q` exhibit weak dependence on the filling, while moves involving changes in the real-space part of configurations tend to be accepted less frequently as the filling is increased.

2. $U/J = 24$, $T/J = 1.0408$

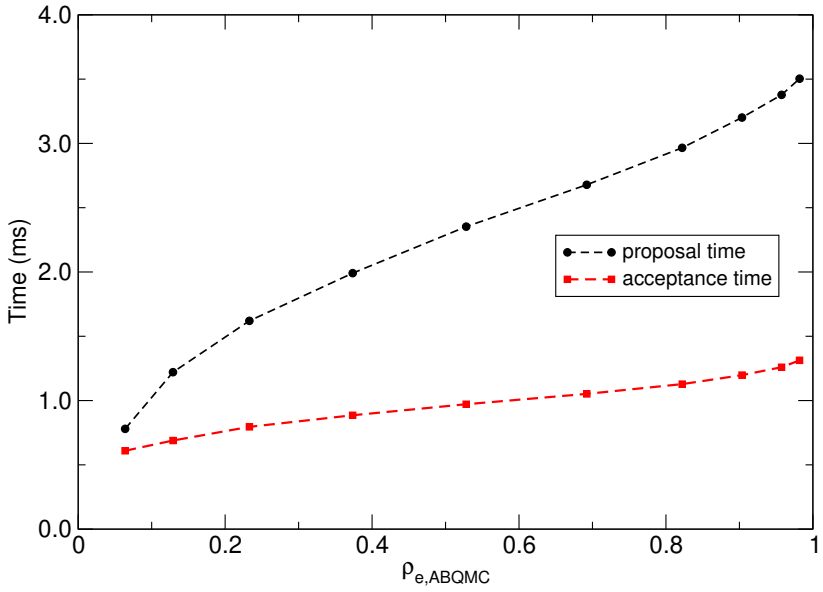

Figure S9. Average time needed to propose (black circles) and accept (red squares) one Monte Carlo update as a function of the ABQMC electron density. The averaging is performed over all updates used in ABQMC simulations to evaluate the equation of state: `add_particle`, `remove_particle`, `spin_flip`, `add_q`, `exchange_q`, `change_r_local`, and `change_r_global`.

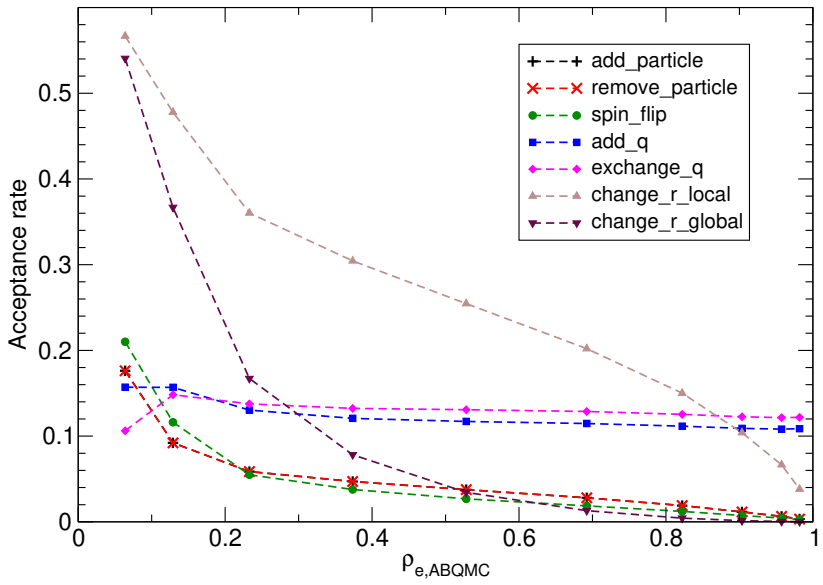

Figure S10. Acceptance rates of individual Monte Carlo updates as a function of the ABQMC electron density. Being inverses of one another, the acceptance rates of moves `add_particle` and `remove_particle` are mutually equal. The acceptance rates of moves `add_q` and `exchange_q` exhibit weak dependence on the filling, while moves `add_particle`, `remove_particle`, `spin_flip`, `change_r_local`, and `change_r_global` tend to be accepted less frequently as the filling is increased.

SV. FPQMC METHOD FOR TIME-DEPENDENT DENSITIES: ADDITIONAL RESULTS

Figure S11(a) summarizes the evolution of charge densities on initially unoccupied sites of a half-filled 4×4 cluster, on which the electrons are initially arranged as summarized in the inset of Fig. S11(b) [the so-called (π, π) density wave]. Figure S11(b) summarizes the extent of the dynamical sign problem, which appears to be somewhat more severe than in the case of the $(\pi, 0)$ density wave discussed in Figs. 8(a) and 8(b) of the main text.

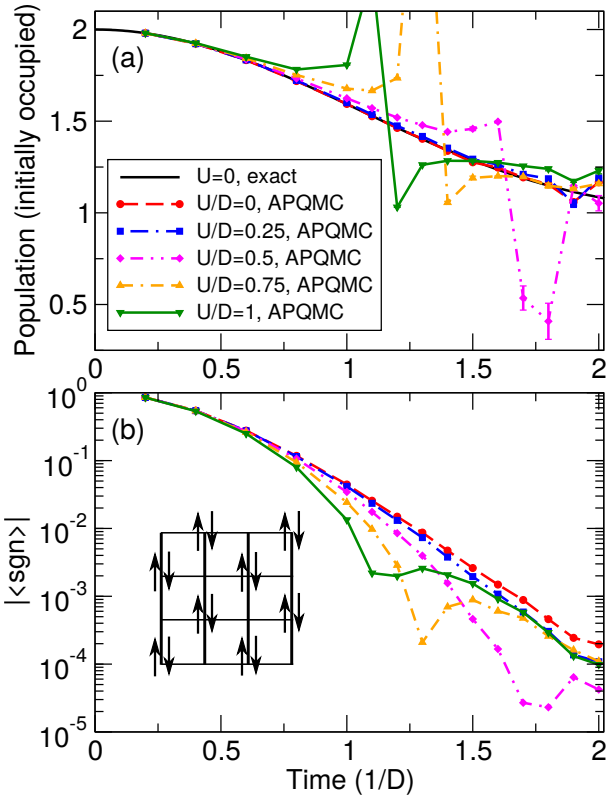

Figure S11. (a) Time-dependent population of sites occupied in the initial CDW state of a 4×4 cluster, which is schematically depicted in the inset of panel (b). FPQMC results using $N_t = 2$ real-time slices (4 slices in total) are shown for five different interaction strengths (symbols) and compared with the noninteracting result (solid line). (b) Magnitude of the average sign as a function of time for different interaction strengths. Color code is the same as in panel (a).

In equilibrium and in the weak-interaction regime, we concluded that the sign problem becomes more pronounced with the filling, see Fig. 4(b) of the main text. Motivated by this finding, we finally study the dynamics of local densities at a smaller filling, see Figs. S12(a1)–S12(b2), which permits us to perform FPQMC simulations on an 8×4 cluster. While the average sign displayed in Fig. S12(a2) is somewhat enhanced with respect to the values reported in Fig. S11(b) and Fig. 8(b) of the main text, the simulated dynamics retains the above-described problems. The average sign decreases with the cluster size, compare the average signs for the noninteracting electrons in Figs. S12(a2) and S12(b2).

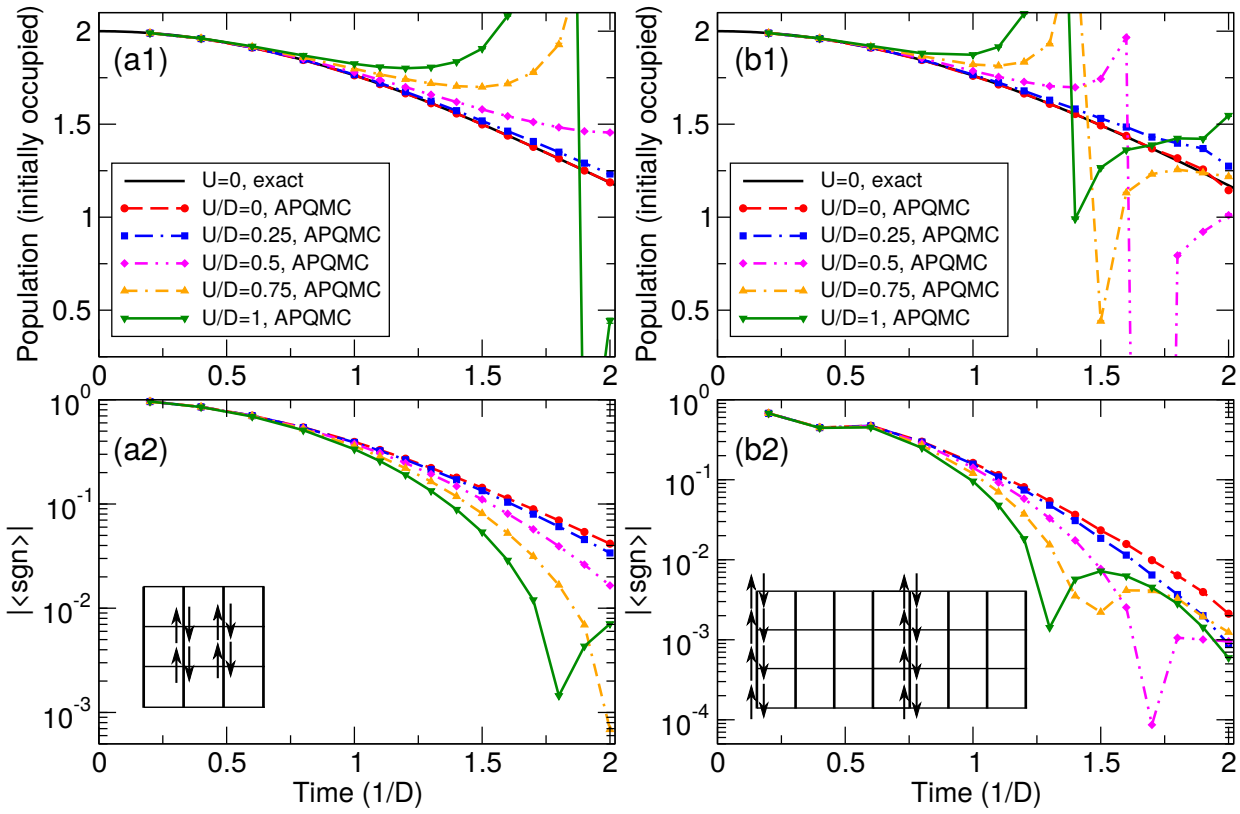

Figure S12. (a1) and (b1) Time-dependent population of sites occupied in the initial state of a 4×4 (a1) and 8×4 (b1) cluster, which is schematically depicted in the inset of panels (a2) and (b2), respectively. FPQMC results using $N_t = 2$ real-time slices (4 slices in total) are shown for five different interaction strengths (symbols) and compared with the noninteracting result (solid line). (a2) and (b2) Time-dependent average sign of the FPQMC simulation for different interaction strengths. Color code is the same as in (a1) and (b1), respectively. Statistical errors are generally smaller than the symbol size.

SVI. ABQMC METHOD FOR TIME-DEPENDENT SURVIVAL PROBABILITY: ADDITIONAL RESULTS

A. Applicability of the ABQMC method to a 4×4 cluster with $N_t = 4$ real-time slices

This section addresses the applicability of the ABQMC method to compute the survival probability of the 16-electron CDW-like/SDW-like state depicted in Fig. 10(a) of the main text when the number of real-time slices is increased from $N_t = 2$ to $N_t = 4$. In Fig. S13 we compare the behavior of the average sign for $N_t = 2$, when we make 3.87×10^{10} steps, and $N_t = 4$, when we make 1.16×10^{10} steps. Increasing the number of real-time slices from 2 to 4 decreases $|\langle \mathrm{sgn} \rangle|$ after 10^{10} MC steps by an order of magnitude. With $N_t = 4$, the stabilization of the average sign takes much more than 10^{10} MC steps, and its overall decrease as the simulation proceeds may be very well described by a power law with the exponent of $-1/2$, see the dashed line in Fig. S13.

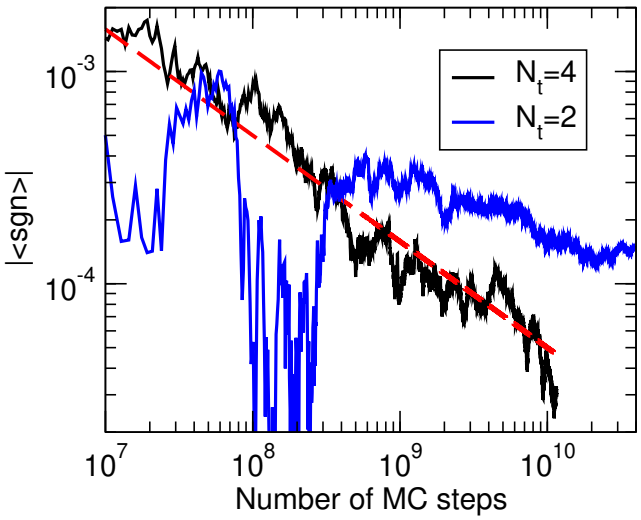

Figure S13. Magnitude of the average sign as a function of the number of MC steps during the ABQMC simulation of the survival probability of the 16-electron CDW/SDW state on a 4×4 square-lattice cluster using $N_t = 2$ and $N_t = 4$ real-time slices. The overall behavior of $|\langle \mathrm{sgn} \rangle|$ for $N_t = 4$ may be fitted very well by the function $5/\sqrt{N_{\mathrm{MC}}}$ that is shown by the dashed line.

B. Applicability of the ABQMC method to an 8×4 cluster with $N_t = 2$ real-time slices

This section addresses the applicability of the ABQMC method to compute the survival probability of a 16-electron initial state on an 8×4 cluster with $N_t = 2$ real-time slices. The initial CDW-like state is schematically depicted in Fig. S14(a), while Fig. S14(b) shows the evolution of the average sign during the MC simulation. We perform 10^{10} MC steps, during which the magnitude of the average sign shows no signals of stabilization, but steadily decreases in a power-law fashion with the exponent $-1/2$, see the dashed line in Fig. S14(b). Even though the final stages of our MC simulation may suggest that $|\langle \mathrm{sgn} \rangle|$ stabilizes on the level of $\sim 4 \times 10^{-5}$, a very noisy behavior of $|\langle \mathrm{sgn} \rangle|$ throughout the simulation casts doubts on such a conclusion. We observe in Fig. S14(b) that $|\langle \mathrm{sgn} \rangle|$ displays pronounced dips whose duration may be as long as a couple of billions of steps, which is in stark contrast with the rather smooth decrease of $|\langle \mathrm{sgn} \rangle|$ observed, e.g., in Fig. S13. These dips suggest that there may be problems with the configuration-space sampling. The dimension of the configuration space of our ABQMC method is much larger than the dimension of the Hilbert space of the model, which is astronomically large for the Hubbard model on an 8×4 cluster. To further illustrate the last point, in Fig. S14(c) we present the survival probability of the initial state in the noninteracting case. In contrast to the 4×4 cluster, for which perfect collapses and revivals in $P(t)$ are observed already on relatively short time scales, there is no such a regular behavior on the 8×4 cluster, see Fig. S14(c). On general grounds, the noninteracting system is bound to display perfect collapses and revivals in $P(t)$, while the time scale on which the pattern in $P(t)$ repeats itself is inversely proportional to the dimension of the system's Hilbert space.

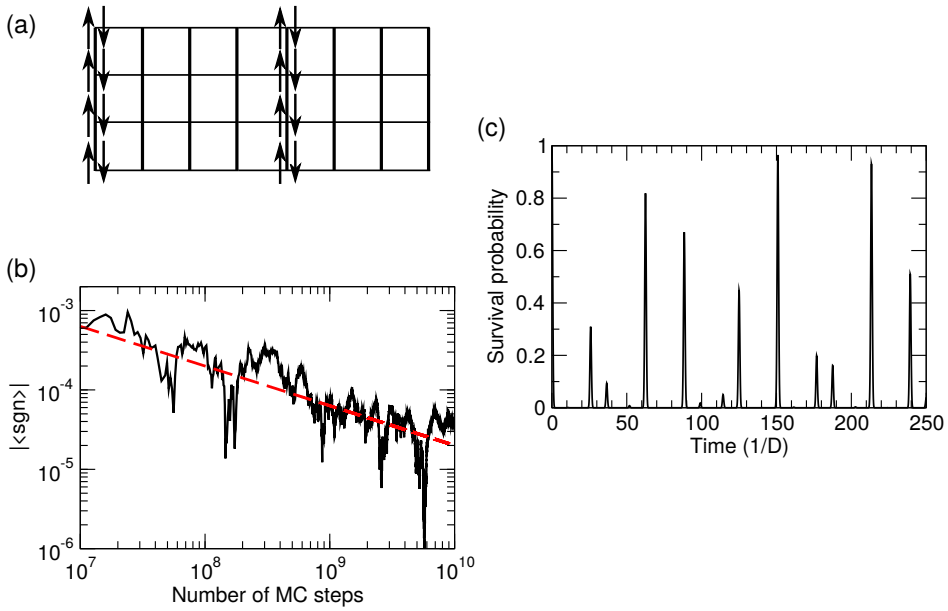

Figure S14. (a) Schematic view of the 16-electron initial state on an 8×4 square-lattice cluster whose survival probability is computed. (b) Magnitude of the average sign as a function of the number of MC steps during the ABQMC simulation of the survival probability of the initial state depicted in (a). $N_t = 2$ real-time slices are used. The overall behavior of $|\langle \mathrm{sgn} \rangle|$ may be fitted very well by the function $2/\sqrt{N_{\mathrm{MC}}}$ that is shown by the dashed line. (c) Time dependence of the survival probability of the initial state depicted in (a) in the noninteracting case $U = 0$. The dimensionality of the system's Hilbert space is so large that no perfect revival in $P(t)$ (which is bound to occur since $U = 0$) is observed up to $Dt = 250$.

C. ABQMC results for the survival probability near the atomic limit

Figure S15 shows $P(t)$ for the 16-electron initial state schematically depicted in Fig. 10(a) of the main text in regimes that are close to the atomic limit. In these regimes, the natural energy unit is U, so that the time is measured in units $1/U$. The time range is chosen on the basis of the results in Figs. (d1)–(e2), which suggest that the ABQMC method with $N_t = 2$ real-time slices produces a qualitatively correct behavior of $P(t)$ up to times $Ut \approx 6$. $P(t)$ exhibits oscillations whose amplitude decreases in time. There is almost no difference between $P(t)$ for $D/U = 0.05$ and 0.1 during the first oscillation, while $P(t)$ for $D/U = 0.2$ is at all times below $P(t)$ for stronger U. While for the strongest U the maxima reached by $P(t)$ are always close to 1, the maxima for weaker U are smaller than 1 and decrease with time. All these observations can be rationalized by an increased importance of the kinetic over the interaction term as U/D is decreased.

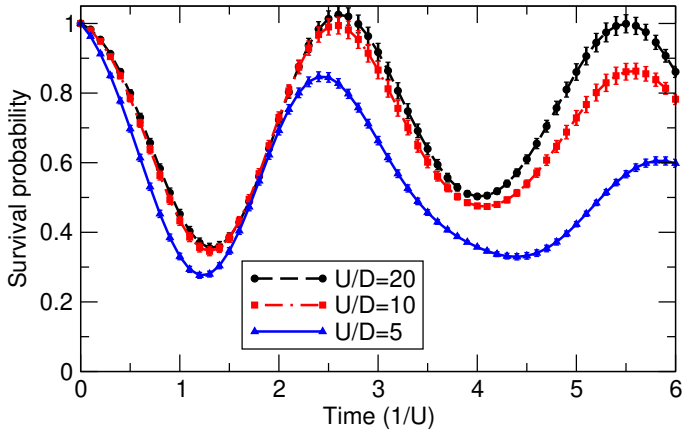

Figure S15. (Color online) Survival-probability dynamics of the 16-electron initial state schematically depicted in Fig. (a) for three values of the interaction strength that are close to the atomic limit.

SVII. ABQMC METHOD TO EVALUATE TIME-DEPENDENT EXPECTATION VALUES ALONG THE KELDYSH–KADANOFF–BAYM CONTOUR

We start from

$$\langle A_a(t)\rangle = \frac{\mathrm{Tr}\left(e^{-\beta H(0)}\, e^{iHt}\, A_a\, e^{-iHt}\right)}{\mathrm{Tr}\left(e^{-\beta H(0)}\right)} \tag{S16}$$

where H is the Hubbard Hamiltonian, while $H(0)$ additionally contains terms that modulate charge or spin density. For example, to simulate the response recorded in Ref. 3, the following $H(0)$ may be appropriate:

$$H(0) = \underbrace{\sum_{\mathbf{k}\sigma} \widetilde{\varepsilon}_{\mathbf{k}}\, n_{\mathbf{k}\sigma} + U \sum_{\mathbf{r}} n_{\mathbf{r}\uparrow} n_{\mathbf{r}\downarrow}}_{H} - \sum_{\mathbf{r}\sigma} v_{\mathbf{r}} n_{\mathbf{r}\sigma} \tag{S17}$$

where $v_{\mathbf{r}}$ is the external harmonic potential that modulates electron density, e.g.,

$$v_{\mathbf{r}} = V_0 \cos(\mathbf{q}\cdot\mathbf{r}). \tag{S18}$$

Inspired by Ref. 3, we assume that $\mathbf{q} = q\mathbf{e}_x$, i.e., we assume that the electron density is modulated along one direction with the wavelength $\lambda = 2\pi/q$. We also assume that $\lambda \le N_x$ and that $N_x \bmod \lambda = 0$, i.e., the cluster's linear dimension along x axis is spanned by an integer number of wavelengths.

There are at least two manners in which the ABQMC method in the presence of external density-modulating potential (at $t < 0$) can be formulated. They differ by the choice of the contributions that are diagonal in the coordinate and momentum representations.

1. The part diagonal in the momentum representation is

   $$[H(0)]_{\mathrm{mom}} = \sum_{\mathbf{k}} \varepsilon_{\mathbf{k}} n_{\mathbf{k}\sigma},$$

   while the part diagonal in the coordinate representation

   $$[H(0)]_{\mathrm{coord}} = U \sum_{\mathbf{r}} n_{\mathbf{r}\uparrow} n_{\mathbf{r}\downarrow} - \sum_{\mathbf{r}\sigma} \mu_{\mathbf{r}} n_{\mathbf{r}\sigma}$$

   contains position-dependent chemical potential $\mu_{\mathbf{r}} = \mu + v_{\mathbf{r}}$. Such a decomposition provides exact results in the atomic limit ($J = 0$) and is expected to provide reasonable results when the electron–electron interaction dominates over the electronic hopping.

2. The part diagonal in some momentum representation is

   $$[H(0)]_{\mathrm{mom}} = \sum_{\mathbf{k}\sigma} \widetilde{\varepsilon}_{\mathbf{k}}\, n_{\mathbf{k}\sigma} - \frac{V_0}{2} \sum_{\mathbf{k}\sigma} \left(c^{\dagger}_{(k_x+q,k_y)\sigma} c_{(k_x,k_y)\sigma} + c^{\dagger}_{(k_x-q,k_y)\sigma} c_{(k_x,k_y)\sigma} \right)$$

   while the part diagonal in the coordinate representation is

   $$[H(0)]_{\mathrm{coord}} = U \sum_{\mathbf{r}} n_{\mathbf{r}\uparrow} n_{\mathbf{r}\downarrow}.$$

   Such a decomposition provides exact results in the noninteracting limit ($U = 0$) and is expected to provide reasonable results when the electronic hopping dominates over the electron–electron interaction. Our further developments will be focused on this decomposition.

The external harmonic potential introduces the coupling between different $\mathbf{k}$ states which results in a reduction of the Brillouin zone along x axis by a factor of λ. The wave vector $\mathbf{k}$ in the full Brillouin zone $[0, 2\pi) \times [0, 2\pi)$ is not a good quantum number anymore. Its role is taken by the wave vector $\widetilde{\mathbf{k}}$ in the reduced Brillouin zone $[0, 2\pi/\lambda) \times [0, 2\pi)$, whose x projection $\widetilde{k}_x$ may assume any of the $n_q = N_x \operatorname{div} \lambda$ allowed values in the interval $[0, 2\pi/\lambda)$ ($p \times 2\pi/N_x$, where $p = 0, \ldots, n_q - 1$) and whose y projection $\widetilde{k}_y$ may assume any of the N_y allowed values in the interval $[0, 2\pi)$ ($p \times 2\pi/N_y$, where $p = 0, \ldots, N_y - 1$). In addition to $\widetilde{\mathbf{k}}$, there is another degree of freedom that will be denoted by

ν_x and that may assume values $0, \ldots, \lambda - 1$. The Hamiltonian H_{mom} has a block-diagonal structure and the blocks defined by the wave vector $\widetilde{\mathbf{k}}$ can be diagonalized separately. There are $n_q N_y$ such blocks and the dimension of each of them is $\lambda \times \lambda$.

The Hubbard Hamiltonian H appears in combination $e^{iHt} \ldots e^{-iHt}$, meaning that the chemical-potential term $-\mu \sum_{\mathbf{r}\sigma} n_{\mathbf{r}\sigma} = -\mu \sum_{\mathbf{k}\sigma} n_{\mathbf{k}\sigma}$ is not effective (we assume that A_a conserves the total particle number, which is a reasonable assumption) and there is no ambiguity regarding the part H_{mom} or H_{coord} to which it should be associated. Therefore, the partition of the Hubbard Hamiltonian in parts that are diagonal in the momentum and coordinate representation is the same as in the main body of the paper

$$H_{\mathrm{mom}} = \sum_{\mathbf{k}\sigma} \varepsilon_{\mathbf{k}} n_{\mathbf{k}\sigma}, \quad H_{\mathrm{coord}} = U \sum_{\mathbf{r}} n_{\mathbf{r}\uparrow} n_{\mathbf{r}\downarrow}.$$

Let us now exploit symmetries to develop as efficient as possible ABQMC algorithm to evaluate Eq. (S16). Since $H(0)$ is not invariant under the bipartite lattice symmetry, we use only the time-reversal symmetry, according to which $\langle A_a(-t) \rangle = \langle A_a(t) \rangle$. Furthermore, we note that both the numerator and the denominator of Eq. (S16) are purely real. Using the strategy described in the main text, one may derive the ABQMC counterpart of Eq. (S16)

$$\langle A_a(t) \rangle = \frac{\sum_{\mathcal{C}} \mathrm{Re}\{\mathcal{D}(\mathcal{C})\}\, e^{-\Delta\tau \varepsilon_{\mathrm{M}}(\mathcal{C})}\, \cos\left\{[\Delta\varepsilon_0(\mathcal{C}) + \Delta\varepsilon_{\mathrm{int}}(\mathcal{C})]\Delta t\right\}\, \mathcal{A}_a(\Psi_{a,l_a})}{\sum_{\mathcal{C}} \mathrm{Re}\{\mathcal{D}(\mathcal{C})\}\, e^{-\Delta\tau \varepsilon_{\mathrm{M}}(\mathcal{C})}} \tag{S19}$$

The configuration $\mathcal{C}$ consists of $2N_t + N_\tau$ many-body states $|\Psi_{k,l}\rangle$ ($l = 1, \ldots, 2N_t + N_\tau$) composed of single-particle momentum eigenstates and $2N_t + N_\tau$ many-body states $|\Psi_{i,l}\rangle$ composed of single-particle coordinate eigenstates. While momenta of states $|\Psi_{k,1}\rangle, \ldots, |\Psi_{k,2N_t}\rangle$ are defined in the full Brillouin zone, states $|\Psi_{k,2N_t+1}\rangle, \ldots, |\Psi_{k,2N_t+N_\tau}\rangle$ have their momenta defined in the reduced Brillouin zone. The symbols $\mathcal{D}(\mathcal{C})$, $\Delta\varepsilon_0(\mathcal{C})$, and $\Delta\varepsilon_{\mathrm{int}}(\mathcal{C})$ are defined as in the main text, while $\varepsilon_{\mathrm{M}}(\mathcal{C})$ is the sum of energies of $2N_\tau$ states along the Matsubara part of the contour, i.e.,

$$\varepsilon_{\mathrm{M}}(\mathcal{C}) = \sum_{l=2N_t+1}^{2N_t+N_\tau} \left[\varepsilon_0(\Psi_{k,l}) + \varepsilon_{\mathrm{int}}(\Psi_{i,l})\right]. \tag{S20}$$

The slice on which the expectation value $\mathcal{A}_a(\Psi_{a,l_a}) = \langle \Psi_{a,l_a} | A_a | \Psi_{a,l_a} \rangle$ is evaluated depends on the representation $a = i, k$ in which the observable A_a is diagonal, so that $l_i = N_t + 1$ and $l_k = N_t$.

The structure of Eq. (S19) is intuitively clear as it is a combination of the ABQMC formula for thermodynamic quantities [Eq. (17) of the main text] and the ABQMC formula for the time-dependent expectation value along the Keldysh contour [Eq. (26) of the main text]. However, since we cannot exploit the bipartite lattice symmetry in this setup, the time-dependent part of the numerator in Eq. (S19) is $\cos\left\{[\Delta\varepsilon_0(\mathcal{C}) + \Delta\varepsilon_{\mathrm{int}}(\mathcal{C})]\Delta t\right\}$ instead of $\cos[\Delta\varepsilon_0(\mathcal{C})\Delta t]\, \cos[\Delta\varepsilon_{\mathrm{int}}(\mathcal{C})\Delta t]$. Configuration weight may be chosen as $w(\mathcal{C}) = |\mathrm{Re}\{\mathcal{D}(\mathcal{C})\}|\, e^{-\Delta\tau \varepsilon_{\mathrm{M}}(\mathcal{C})}$ and Eq. (S19) is recast as

$$\langle A_a(t) \rangle = \frac{\langle \mathrm{sgn}(\mathcal{C})\, \cos\left\{[\Delta\varepsilon_0(\mathcal{C}) + \Delta\varepsilon_{\mathrm{int}}(\mathcal{C})]\Delta t\right\}\, \mathcal{A}_a(\Psi_{a,l_a}) \rangle_w}{\langle \mathrm{sgn}(\mathcal{C}) \rangle_w}. \tag{S21}$$

Markov-chain MC evaluation of Eq. (S21) suffers from the sign problem that does not depend on time t (it is not dynamical). Still, it becomes more pronounced when the cluster size N_c or the number of slices (N_t and N_τ) are increased. Similarly to equilibrium ABQMC calculations, the weight $w(\mathcal{C})$ depends on all model parameters (U, T, μ, V_0, t). Therefore, the calculations for different values of these parameters have to be performed using different Markov chains, which is different from the computation of $P(t)$ or $\langle A_a(t) \rangle$ starting from a pure state $|\psi(0)\rangle$.

The application of conservation laws on the Kadanoff–Baym contour is somewhat more involved than on simpler contours studied in the main body of the paper. The particle-number conservation demands that all the many-body states constituting configuration $\mathcal{C}$ have the same number of spin-up and spin-down electrons. We discuss the momentum conservation under the assumption that the observable A_a is diagonal in the coordinate representation (e.g., $A_i = \sum_\sigma n_{\mathbf{r}\sigma}$). From the main text, we know that the momentum conservation along the horizontal parts of the contour (Keldysh branch) is broken into two conservation laws that are satisfied separately on the forward and backward branch. In other words, the momenta (in the full Brillouin zone!) of N_t momentum-space states $|\Psi_{k,1}\rangle, \ldots, |\Psi_{k,N_t}\rangle$ on the forward branch are all equal to $\mathbf{K}_{\mathrm{fwd}}$, while the momenta of N_t momentum-space states $|\Psi_{k,N_t+1}\rangle, \ldots, |\Psi_{k,2N_t}\rangle$ on the backward branch are all equal to $\mathbf{K}_{\mathrm{bwd}}$. In contrast to the situation encountered in the main text, $\mathbf{K}_{\mathrm{fwd}}$ and $\mathbf{K}_{\mathrm{bwd}}$ are not completely independent because states $|\Psi_{k,1}\rangle$ and $|\Psi_{k,2N_t}\rangle$ are "in contact" with states $|\Psi_{k,2N_t+N_\tau}\rangle$ and $|\Psi_{k,2N_t+1}\rangle$ on the Matsubara branch. Therefore, the relation between $\mathbf{K}_{\mathrm{fwd}}$ and $\mathbf{K}_{\mathrm{bwd}}$ is determined by the momentum-conservation law along the Matsubara branch, which is formulated in the reduced Brillouin zone. Namely,

the momenta (in the reduced Brillouin zone!) of N_τ momentum-space states $|\Psi_{k,2N_t+1}\rangle, \ldots, |\Psi_{k,2N_t+N_\tau}\rangle$ are all equal to $\widetilde{\mathbf{K}}_{\mathrm{M}}$. The momenta $\mathbf{K}_{\mathrm{fwd}}$, $\mathbf{K}_{\mathrm{bwd}}$, and $\widetilde{\mathbf{K}}_{\mathrm{M}}$ are related as follows:

$$\mathbf{K}_{\mathrm{fwd}} \cdot \mathbf{e}_y = \mathbf{K}_{\mathrm{bwd}} \cdot \mathbf{e}_y = \widetilde{\mathbf{K}}_{\mathrm{M}} \cdot \mathbf{e}_y,$$

$$\frac{\mathbf{K}_{\mathrm{fwd}} \cdot \mathbf{e}_x}{2\pi/N_x} \bmod \frac{N_x}{\lambda} = \frac{\widetilde{\mathbf{K}}_{\mathrm{M}} \cdot \mathbf{e}_x}{2\pi/N_x}, \quad \frac{\mathbf{K}_{\mathrm{bwd}} \cdot \mathbf{e}_x}{2\pi/N_x} \bmod \frac{N_x}{\lambda} = \frac{\widetilde{\mathbf{K}}_{\mathrm{M}} \cdot \mathbf{e}_x}{2\pi/N_x}$$

Due to the more complicated momentum-conservation law, MC updates presented in Sec. SI have to be amply modified. Instead of describing modified MC updates in detail, we demonstrate the correctness of our implementation by benchmarking it on small clusters. Motivated by Ref. 3, we limit the discussion to the electron occupation dynamics on individual sites.

We start from the noninteracting electrons, where already $N_\tau = 1$ imaginary-time slice and $2N_t = 2$ real-time slices ($2N_t + N_\tau = 3$ slices in total) are expected to reproduce the exact result. Trivial as they may seem, the benchmarks on the noninteracting case are quite important, because densities of individual sites are expected to display nontrivial oscillatory behavior. The fact that our ABQMC results reproduce these oscillations quite accurately strongly suggests that our implementation is correct. In Fig. S16 we present results for the Hubbard dimer initially subjected to the external density-modulating field $v_{r_x} = V_0 \cos(\pi r_x)$ with $r_x = 0, 1$. Figure S17 displays results for the Hubbard tetramer initially subjected to the external density-modulating field of wavelength $\lambda = 4$, $v_{r_x} = V_0 \cos(\pi r_x/2)$, with $r_x = 0,\ 1,\ 2,\ 3$. Figure S18 displays results for the Hubbard tetramer initially subjected to the external density-modulating field of wavelength $\lambda = 2$, $v_{r_x} = V_0 \cos(\pi r_x)$, with $r_x = 0,\ 1,\ 2,\ 3$.

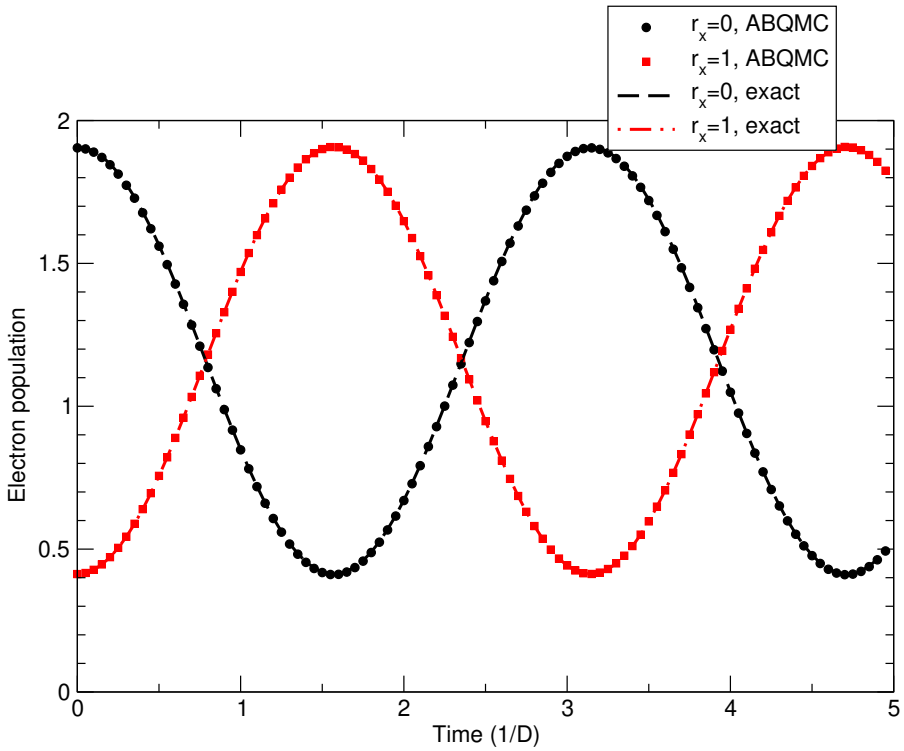

Figure S16. Time-dependent site populations of the Hubbard dimer with the following values of model parameters: $\mu/D = 1.3$, $V_0/D = 2$, $U = 0, T/D = 0.57$. The external potential at $t < 0$ is $v_{r_x} = V_0 \cos(\pi r_x)$ with $r_x = 0, 1$.

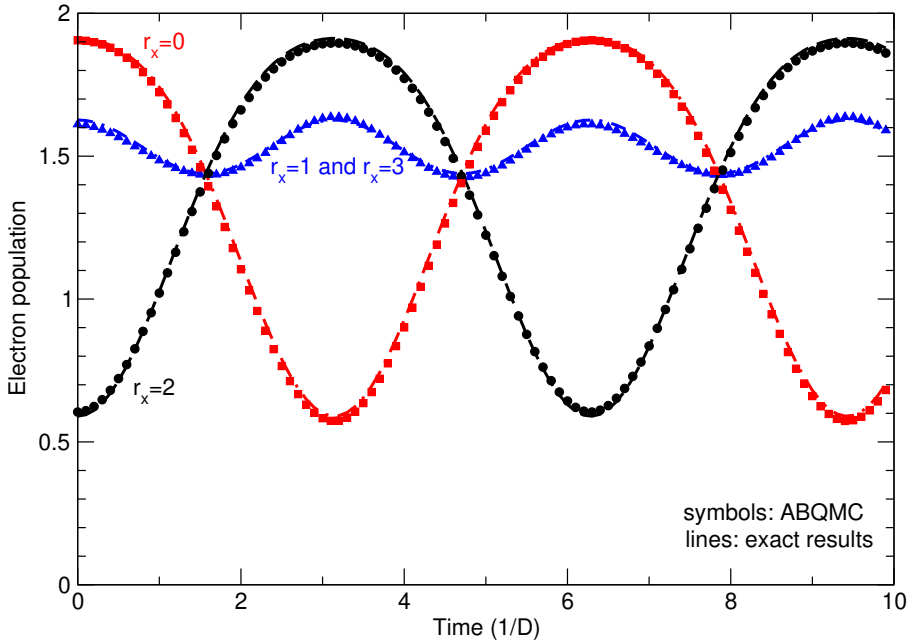

Figure S17. Time-dependent site populations of the Hubbard tetramer with the following values of model parameters: $\mu/D = 0.65$, $V_0/D = 1$, $U = 0$, $T/D = 0.285$. The external potential at $t < 0$ is $v_{r_x} = V_0 \cos(\pi r_x/2)$ with $r_x = 0,\ 1,\ 2,\ 3$.

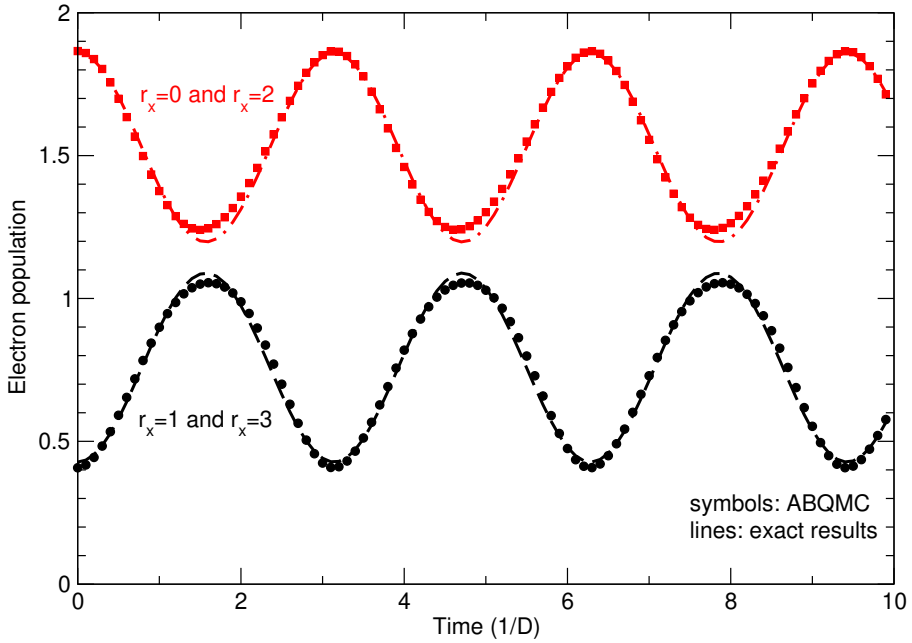

Figure S18. Time-dependent site populations of the Hubbard teteramer with the following values of model parameters: $\mu/D = 0.65$, $V_0/D = 1$, $U = 0$, $T/D = 0.285$. The external potential at $t < 0$ is $v_{r_x} = V_0 \cos(\pi r_x)$ with $r_x = 0,\ 1,\ 2,\ 3$.

We conclude this section by applying the ABQMC algorithm to interacting electrons. We first discuss the Hubbard dimer in the canonical ensemble, where we can obtain converged results with as many as $2N_t + N_\tau = 12$ slices in total at half-filling ($N_\uparrow = N_\downarrow = 1$). The results are presented in Fig. S19. We observe that ABQMC results qualitatively reproduce the exact result in the whole time window considered. The quantitative agreement is reasonable up to $Dt \approx 2$. Figure S20 presents results for the Hubbard tetramer in the grand-canonical ensemble, where we obtain converged results using only $N_t = 1$ and $N_\tau = 2$. Further increase in N_t reduces the average sign by orders of magnitude: for $N_t = 1$, $N_\tau = 2$ we obtain $|\langle \mathrm{sgn} \rangle| = 1.2 \times 10^{-2}$, while for $N_t = 2$, $N_\tau = 2$ we find $|\langle \mathrm{sgn} \rangle| \sim 10^{-4}$.

While $N_\tau = 2$ is enough to reproduce equilibrium populations in the external field at $t = 0$, a single real-time slice leads to the quantitative agreement between the ABQMC and exact results only at shortest times.

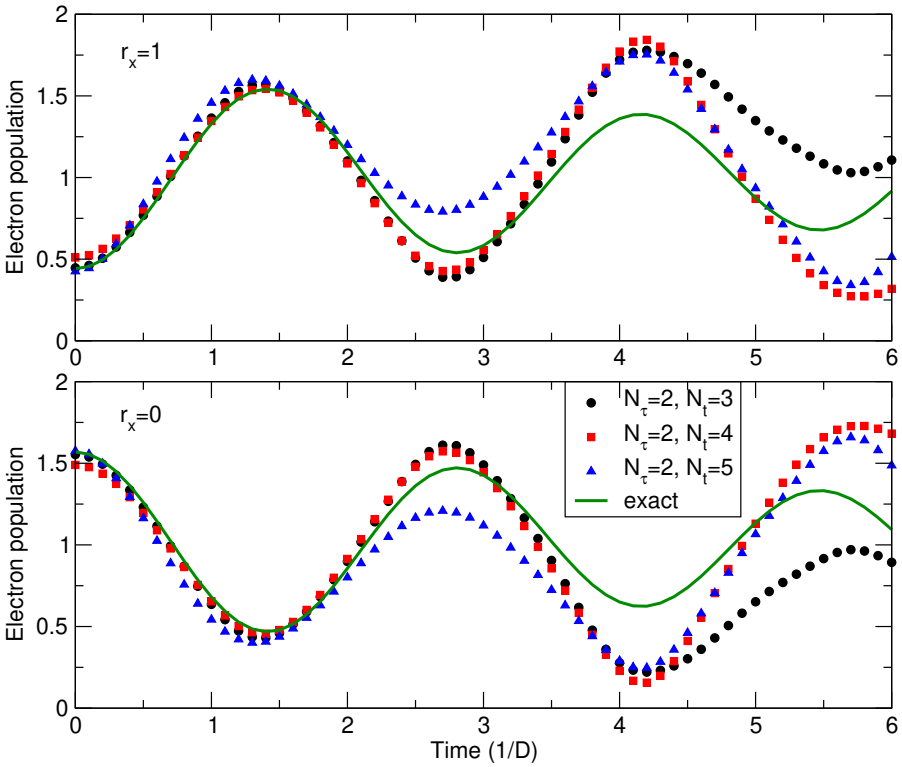

Figure S19. Dynamics of electron populations on individual sites of the Hubbard dimer that at $t < 0$ is subjected to the density-modulating potential $v_{r_x} = V_0 \cos(\pi r_x)$ with $r_x = 0,\ 1$. We work in the canonical ensemble with $N_\uparrow = N_\downarrow = 1$. The model parameters assume the following values: $V_0/D = 1$, $U/D = 0.6$, $T/D = 0.45$.

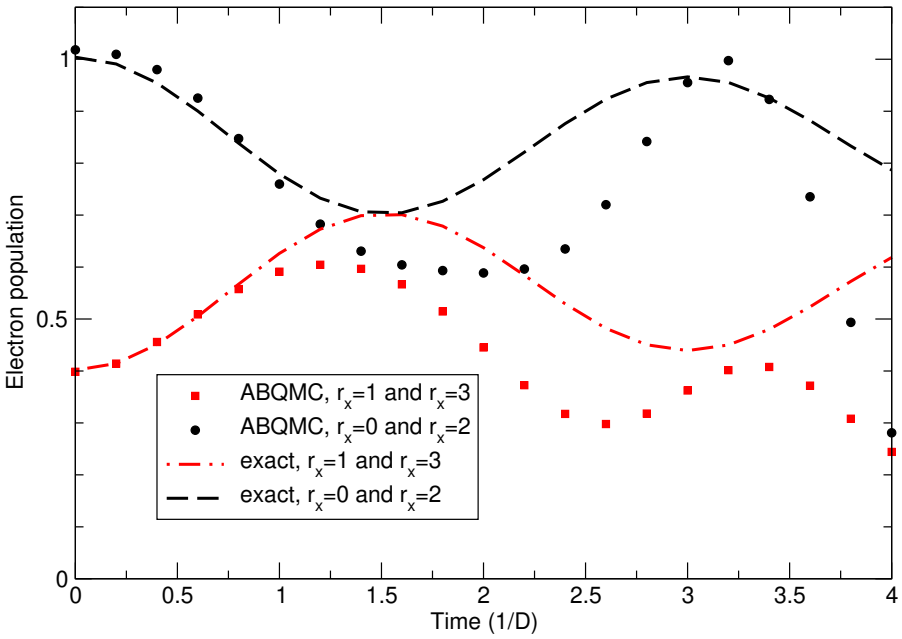

Figure S20. Dynamics of electron populations on individual sites of the Hubbard tetramer that at $t < 0$ is subjected to the density-modulating potential $v_{r_x} = V_0 \cos(\pi r_x)$ with $r_x = 0$, 1, 2, 3. We work in the grand-canonical ensemble with $N_t = 1$, $N_\tau = 2$ ($2N_t + N_\tau = 4$ slices in total), and the following values of model parameters: $\mu/D = -0.325$, $V_0/D = 0.5$, $U/D = 0.5$, $T/D = 0.5$.

REFERENCES

[1]This follows from the cyclic invariance under the trace.
[2]E. Khatami and M. Rigol, "Thermodynamics of strongly interacting fermions in two-dimensional optical lattices," Phys. Rev. A **84**, 053611 (2011).
[3]P. T. Brown, D. Mitra, E. Guardado-Sanchez, R. Nourafkan, A. Reymbaut, C.-D. Hébert, S. Bergeron, A.-M. S. Tremblay, J. Kokalj, D. A. Huse, P. Schauss, and W. S. Bakr, "Bad metallic transport in a cold atom Fermi-Hubbard system," Science **363**, 379–382 (2019).